Journal of the Optical Society of America B
OPTICAL PHYSICS

Double split-loop resonators as building blocks of metasurfaces for light manipulation: bending, focusing, and flat-top generation

Ali Forouzmand, Shifei Tao, Samad Jafar-Zanjani, Jierong Cheng, Mohammad Mahdi Salary, and Hossein Mosallaei*

Computational EM and Physics Laboratory, Electrical and Computer Engineering Department, Northeastern University, Boston, Massachusetts 02115, USA
**Corresponding author: Hosseinm@ece.neu.edu*

Received 9 December 2015; revised 28 April 2016; accepted 18 May 2016; posted 19 May 2016 (Doc. ID 255430); published 7 June 2016

In this paper, we demonstrate the concept of simultaneous controlling of the phase and the polarization handedness of a circularly polarized (CP) incident beam over an array of bilayer double split-loop resonators (DSLRs). The physical parameters are optimized by means of the finite-difference time-domain method in such a way that each unit-cell exhibits the half-wave-plate response. By simply rotating the unit-cell, the phase shift of the transmitted cross polarized beam can be controlled in the range of 0 – 2π without any restrictions. This plasmonic metasurface provides optimal cross polarization transmission efficiency (>70%) at 1.55 μm wavelength. An array of DSLRs with helicity dependency and spatially varying phase response offers the possibility of designing anomalous bending and bifunctional (convergence/divergence) metasurfaces in which the bending direction and convergence/divergence feature can be directly controlled by the handedness of the impinging CP wave. Furthermore, a metalens with the capability of converting a CP Gaussian beam into a uniform irradiance profile (flat-top beam) is designed, and the performance of structure is evaluated in detail. All the designs are composed of the same DSLR elements with space-variant orientations. © 2016 Optical Society of America

OCIS codes: (160.3918) Metamaterials; (250.5403) Plasmonics; (310.6628) Subwavelength structures, nanostructures; (350.4600) Optical engineering; (130.5440) Polarization-selective devices; (050.1965) Diffractive lenses.

http://dx.doi.org/10.1364/JOSAB.33.001411

1. INTRODUCTION

The development of artificially engineered metamaterials (MTMs) stems from the recent demonstration of their unique electromagnetic properties including negative refraction [1–3], subdiffraction imaging [4–8], and invisibility [9–12]. In comparison to the traditional lenses and imaging devices, MTMs provide an alternative approach to wave manipulation with reduced thickness and higher resolution. In spite of these advances in imaging devices and metalenses, the implementation of MTMs is severely challenging due to their high sensitivity to loss and the fabrication complexity in three-dimensional (3D) form. In particular, the lens thickness, as an inevitable parameter to provide the required spatial variation of refraction effects along the lens, strongly restricts the compactness. In order to surpass the aforementioned bounds, the investigation of equivalent 2D surfaces, or metasurfaces (MTSs), capable of performing the same functionality has been prompted. MTSs, which can be realized by nanopatterning thin films, can offer a wide range of potential applications in the design of controllable surfaces, novel waveguiding structures, absorbers, miniaturized cavity resonators, and frequency selective surfaces. MTSs are constructed from functional resonant optical nanoantennas. The resonant characteristic plays an important role in controlling the amplitude, phase, and polarization of the scattered light. The optical properties of each unit-cell can be tuned through choices of the nanoantenna material, geometry, physical dimensions, and orientation. By placing nanoantennas with different scattering functionalities on a surface, space-variant MTSs are obtained which provide more degrees of freedom in manipulating optical wavefronts.

Recently, the phenomenon of phase discontinuities with exploitation of the electromagnetic MTSs has attracted considerable attention, and it has been used for novel and intriguing applications by tailoring the phase distribution of MTSs such as flat lenses [13–15], optical information processing and analog computation [16,17], manipulation of polarization state [18,19], wavefront engineering in reflection/transmission modes [20–24], manipulating orbital angular momentum of

light [25], and 2D/3D holography [26–30]. As described by the generalized Snell's law [20,21], the physical mechanism behind this technique can be described as an abrupt phase change which mainly has taken place at the interface of the lens. Therefore, the recent realization of MTSs or MTMs of reduced dimensionality indeed can replace the traditional lenses in which the required phase has been obtained by the phase accumulation along the lens.

So far, the majority of proposed MTSs have been focused on manipulation of the phase and amplitude of the linearly polarized waves [13,14,17,18,22,23,28–31]. Here, we are interested in controlling the transmission phase for the cross polarization of the circularly polarized (CP) waves as it provides a better mean for phase control [32–34]. We will focus on the design and optimization of thin double-layer split-loop resonators (DSLRs), which can change the handedness of a CP incident wave (similar to a half-wave plasmonic plate) and simultaneously introduce an orientation-related phase shift from 0 to 2π for the transmitted field, while efficient transmission amplitude is also achieved. The desired characteristics—same transmission amplitudes and 180° phase shift between the two orthogonal linearly polarized incident beams (parallel and perpendicular to the optical axis)—can be realized by tuning the resonance of each split-loop resonator (SLR) through altering the inner and outer radii, thickness, and size of the gap. Consequently, the rotation of the DSLRs gains an arbitrary phase shift for the CP incident wave based on the Parancharatnam–Berry (PB) geometric phase manipulation [35,36]. In Section 2, we investigate the transmission performance of periodic arrays of such inclusions and their optimal performance properties in such a way that high cross transmission (>70%) and low cotransmission (<30%) for CP incident wave as a desired property is guaranteed. In comparison to the other recently proposed planar MTSs, the most significant advantage of our proposed lens resides in the fact that its operating principle is based on the phase shift obtained by rotation of the elements without any modification of the geometrical dimensions. This straightforward technique can generate a smooth phase shift from 0 to 2π and obviates the need for exhaustive parametric studies. Furthermore, the optimization has been carried out in such a way that the unit-cell guarantees the optimal trade-off between the transmission performance and the compactness. In Section 3, the unit-cells with different geometrical orientations are placed on a surface to create space-variant MTSs. Our study reveals that the phase discontinuity on the lens can be metamorphosed by controlling the helicity of the CP wave. We leverage this bifunctionality of the proposed lens with respect to the handedness of the incident polarization in order to realize different light manipulations and optical beam shaping techniques such as the anomalous wavefront bending and converging/diverging of a CP plane wave. Moreover, we employ the theory of lossless beam shaping to design a MTS for converting a CP Gaussian beam into a beam with a uniform irradiance. This kind of beam, which is nearly constant over a specified area, is commonly called a flat-top beam. The proposed beam shaper integrates phase filter and focusing lens elements into a single optical metalens which offers simple fabrication and a compact optical system design. In addition, a collimated uniform irradiance beam is realized by utilizing a conjugate phase lens at the target plane of the optical system. Thus, the uniform beam can propagate for longer distances beyond the target plane [37–39]. The conclusion is drawn in Section 4.

2. PLASMONIC MTS ELEMENT DESIGN

We are interested in designing a MTS which enables us to control the phase shift of the transmitted field and convert the left-handed CP (LHCP) wave to a right-handed CP (RHCP) wave and vice versa, at the same time. This functionality can be achieved by exploiting a structure with half-wave-plate response. Recently, the characteristics of the multimaterial concentric loop nanoantennas in low and high coupling schemes have been studied by Mosallaei's group in [40,41]. In particular, two concentric loops which are made of various materials—silver, gold, indium tin oxide, and aluminum-doped zinc oxide—have been investigated, and a framework to control the resonances and design low-coupled and high-coupled loop MTSs by tuning the physical parameters has been presented. Following this idea, we consider a bilayer DSLR as shown in Fig. 1. Figure 1 illustrates the schematic diagram of one unit-cell of a periodic quadratic structure with the lattice constant of P consisting of two layers of DSLRs which are separated by a dielectric slab (SiO_2) with permittivity of $\epsilon_h = 2.2$ and thickness of h. The inner loop of the investigated structure has inner radius of R_1, outer radius of R_2, gap with opening angle of α_1, and thickness of t. The outer loop has inner radius of R_3, outer radius of R_4, and gap with opening angle of α_2. The two layers of DSLRs have exactly the same geometry. The DSLRs are made of silver, and the optical behavior of this noble metal is described through its dispersive permittivity, which can be approximated with a Drude model in the near-infrared (NIR) spectral region as

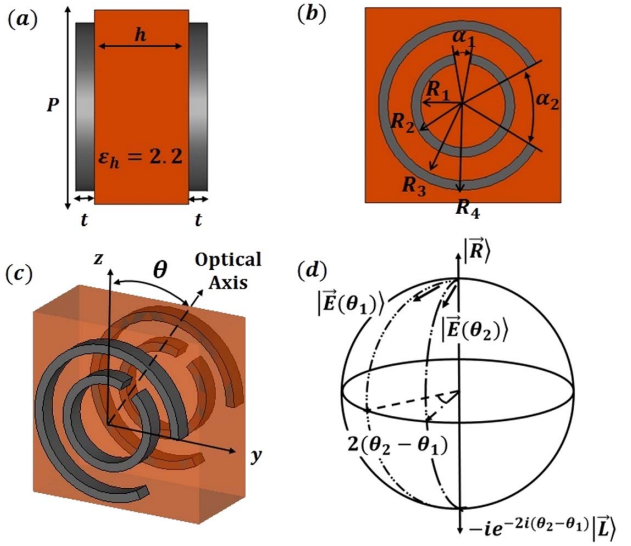

Fig. 1. Schematic of the unit-cell of a period of bilayer DSLRs: (a) x–z plane (cross-sectional view), (b) y–z plane (top view), and (c) 3D view. (d) Illustration of the principle of PB phase on the Poincaré sphere.

$$\epsilon_{Ag}(\omega) = \epsilon_0\left(\epsilon_\infty - \frac{\omega_p^2}{\omega(\omega + i\Gamma)}\right), \quad (1)$$

where $\epsilon_\infty = 5$, the plasma frequency is $\omega_p = 2\pi \times 2.175$ PHz, and the collision frequency is $\Gamma = 2\pi \times 4.35$ THz [42,43]. The silver DSLR configuration can be experimentally implemented by using the well-known method of electron-beam lithography, followed by e-beam silver evaporation and lift-off procedures [44–49].

Here, we describe the behavior of this optical element based on the PB geometric phase manipulation. It has been shown that if the polarization of an incident light beam traverses a closed path in the space of polarization states of light (Poincaré sphere), it acquires a geometric phase in addition to the dynamic phase from the accumulated path length. The final state differs from the initial state by a phase factor equal to half of the solid angle encompassed by the path on Poincaré sphere ($|2(\theta_2 - \theta_1)|$) [35,36]. Figure 1(d) illustrates the concept of PB on the Poincaré sphere. It can be concluded that by arbitrarily rotating a MTS with half-wave-plate functionality by θ, a CP incident light beam will be fully transformed to a beam of opposite helicity (from purely RHCP to LHCP or vice versa) and influenced with a geometric phase equal to $\pm 2\theta$. By controlling the local orientation of the PB elements between 0 to π, any desired phase modification can be achieved in the range of 0 to 2π.

For an incident plane wave $|E_{in}\rangle$ with an arbitrary polarization state, the transmitted field of the PB elements $|E_{out}\rangle$ can be calculated by using the Jones calculus as [33,50]

$$\begin{aligned} |E_{out}\rangle &= \sqrt{\eta_E}|E_{in}\rangle + \sqrt{\eta_R}e^{+i2\theta}|R\rangle + \sqrt{\eta_L}e^{-i2\theta}|L\rangle, \\ \eta_E &= \left|\frac{1}{2}(t_y + t_z e^{i\varphi})\right|^2, \\ \eta_R &= \left|\frac{1}{2}(t_y - t_z e^{i\varphi})\langle L|E_{in}\rangle\right|^2, \\ \eta_L &= \left|\frac{1}{2}(t_y - t_z e^{i\varphi})\langle R|E_{in}\rangle\right|^2, \end{aligned} \quad (2)$$

where $|R\rangle = (1 \quad 0)^T$ and $|L\rangle = (0 \quad 1)^T$ denote the RHCP and LHCP unit vectors, respectively. η_E, η_R, and η_L are the magnitudes of the coupling efficiencies to the different polarization orders. Here, we use Dirac bracket notation, where $\langle\cdot|\cdot\rangle$ denotes an inner product. t_z and t_y are the transmission coefficients for the light polarized parallel and perpendicular to the optical axis [in Fig. 1(c)], and ϕ is the phase retardation between these linear polarization states. From Eq. (2), it is apparent that the emerging beam comprises three polarization states, which can be described as follows: the first remains with the original polarization state and the phase of the incident beam, the second is RHCP with a phase modification of $+2\theta$, and the third is LHCP with a phase modification of -2θ.

When the incident wave is purely LHCP (RHCP), the efficiency of $\eta_L(\eta_R)$ is equal to zero. Therefore, Eq. (2) indicates that the transmitted field comprises two polarization orders. The first term has the phase and polarization state similar to the incident wave, and the second term (third term) exhibits opposite handedness and experiences a phase pickup equal to $\pm 2\theta$, in which the sign should be selected with respect to the helicity of the incident CP wave and the rotation direction of the unit-cell. For the ideal case of $t_y = t_z = 1$ and $\phi = \pi$, an incident wave with right-handed polarization $|R\rangle$ leads to total polarization state conversion and results in a transmitted field as [36]

$$|E_{out}\rangle = e^{-i2\theta}|L\rangle. \quad (3)$$

Equation (3) can clearly demonstrate that an incident CP wave will change its handedness of polarization and simultaneously acquire a phase shift of -2θ. In order to design a MTS that operates with this functionality at $\lambda = 1550$ nm ($f = 193.5$ THz), the structural parameters are selected by a parametric analysis as follows: $P = 415$ nm, $h = 200$ nm, $R_1 = 90$ nm, $R_2 = 110$ nm, $R_3 = 160$ nm, $R_4 = 180$ nm, $\alpha_1 = 20°$, $\alpha_2 = 60°$, and $t = 40$ nm.

The finite-difference time-domain (FDTD) method is utilized to simulate the transmission characteristics of the bilayer DSLRs. The periodic boundary condition is applied at y- and z-directions, and the absorbing boundary condition is applied to the x-direction. The amplitude and phase of the transmission coefficients versus frequency with rotation angle of $\theta = 0$ are plotted in Fig. 2. It is observed from Figs. 2(a) and 2(b) that the amplitudes of both y-directed and z-directed components are equal (the insertion loss is 2.88 dB) and phase difference between them is 176.64° (≈180°) at the operating frequency of $f = 193.5$ THz. It is worth noting that although silver has some absorption at the operating frequency, the structure could satisfy closely the aforementioned conditions of a lossless half-wave plate.

There are several interesting points about the corresponding MTS. The bilayer DSLRs are utilized to overcome the challenge of intrinsically low transmission amplitude of the single-layer unit-cell. In addition, the double layer can guarantee the possibility

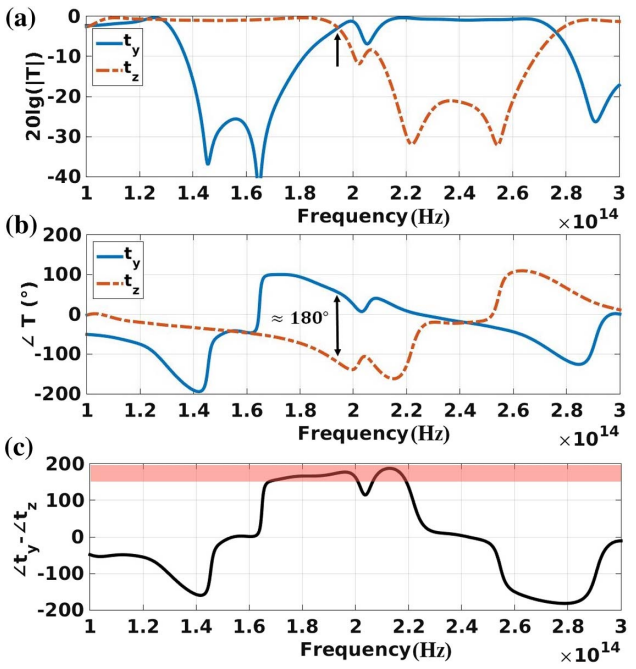

Fig. 2. (a) Amplitude and (b) phase of the transmission coefficients for the y- and z-polarized incident waves. (c) Phase difference between transmitted E_y and E_z. The results are obtained for the reference unit-cell with the rotation angle of $\theta = 0$.

of achieving the required phase difference ($\angle t_y - \angle t_z = 180°$) [51,52]. It has been shown that the transmission response of the double layer can cover a wider range of phase differences between the incident and transmitted fields ($\angle t_y$ and $\angle t_z$) and thus can facilitate the design procedure, as shown in Figs. 3(c) and 3(d) in [53]. Although due to the frequency dispersion, the ideal half-wave-plate conditions can be met only at the single frequency of $f = 193.5$ THz, and the phase difference of the transmitted linearly polarized components smoothly changes around the operating frequency with the phase bandwidth of 173–218 THz. This region ($180° \pm 20°$) is shown by the shadowed area in Fig. 2(c). On the other hand, the ratio of the amplitudes of the transmitted linearly polarized components is within the range of 0.7–1.3 in 191.1 to 196.4 THz. It can be concluded that the acceptable operating frequency range is 191.1 to 196.4 THz in which the performance of the MTS as a half-wave plate is still satisfactory. The optimization has been carried out in such a way that we obtain the optimal trade-off between transmission performance and the compactness of the unit-cell. The total thickness of the lens is chosen as 280 nm, which is lower than $\lambda/5.5$ at the operating frequency.

It has been discussed in [54–57] that an incident electromagnetic wave can excite the magnetic resonance of a SLR while the external magnetic field is perpendicular to the SLR plane (the propagation direction is parallel to the SLR) or if the incident electric field is oriented along the direction in which the SLR does not have mirror symmetry (the propagation direction is perpendicular to the SLR). The latter case corresponds to a weaker resonance, which takes place due to the electric coupling of the incident EM wave to the magnetic resonance of the SLR. In order to illustrate this fact, we first treat the SLRs separately and focus on the inner split loop. Let us assume that an incident electric field with polarization perpendicular to the gap of the inner SLR (E_z) is illuminated to the structure; the near-field distribution is depicted in Fig. 3(a). Since the incident light preserves the symmetry of the inner SLR, currents with opposite directions are induced in each half-arm, which causes the electric field in the gap to vanish, and no resonance will be observed. On the other hand, the outer split loop has been rotated counterclockwise in our design by 90° relative to the inner split loop. Therefore, the outer loop does not have mirror symmetry with respect to the incident electric field direction, which causes the excitation of the magnetic resonance. Figure 3(b) illustrates the near-field distribution when the structure is illuminated by the electric field with polarization perpendicular to the outer SLR's gap (E_y). It is clearly shown that the electric field is strongly confined at the inner split loop's gap, and the resonance occurs. However, the outer split loop, due to the mirror symmetry with respect to the incident electric field direction, does not experience a resonance (the electric field vanishes in the gap). It can be concluded that two distinct resonances occur when the structure is illuminated by two orthogonal linear polarizations perpendicular to the gaps of SLRs, and each resonance can be controlled independently.

To further demonstrate the prediction of Eqs. (2) and (3) regarding the relation between the geometric phase modifications of the transmitted electric field and the variation of the orientation angle of the unit-cell, the simulated amplitude and phase response of the structure when illuminated by a CP wave are plotted versus rotation angle $\theta = [0, \pi/2]$ in Fig. 4 (the FDTD results for the other rotation angles, $\theta = [-\pi/2, 0]$, have a great agreement with the theoretical approach as well). The transmission coefficients of CP waves can be converted from the linear transmission coefficients using the Jones matrix method as discussed in [58–62]. In Fig. 4, "In" and "Out" correspond to the incident and transmitted CP waves, respectively. For the transmitted components with the opposite handedness [LHCP–RHCP and RHCP–LHCP], the full-wave simulation results prove the claim that the CP wave passing through the structure gains a phase shift which is equal to twice the rotation angle of the unit-cell [as shown in Fig. 4(b)], which is consistent with the theoretical expectations in Eqs. (2) and (3). In addition, it should be mentioned that for cotransmitted fields (LHCP–LHCP and RHCP–RHCP), there is no phase change regardless of the unit-cell rotation.

In this design, it is desirable to attain a low insertion loss and a large polarization extinction ratio (i.e., the level of cross-transmission to cotransmission). FDTD simulation results

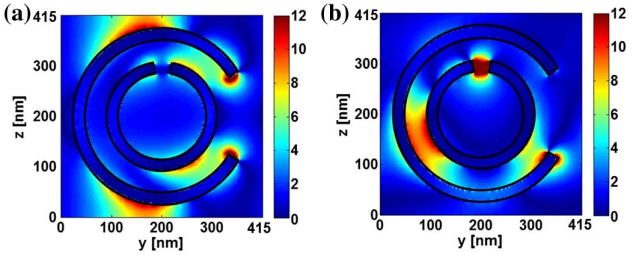

Fig. 3. Near field distribution of the electric field around the DSLRs at the operating frequency of $f = 193.5$ THz. Two different illumination polarizations are considered: (a) E_z and (b) E_y. The distributions are computed in the y–z plane through the top of the substrate.

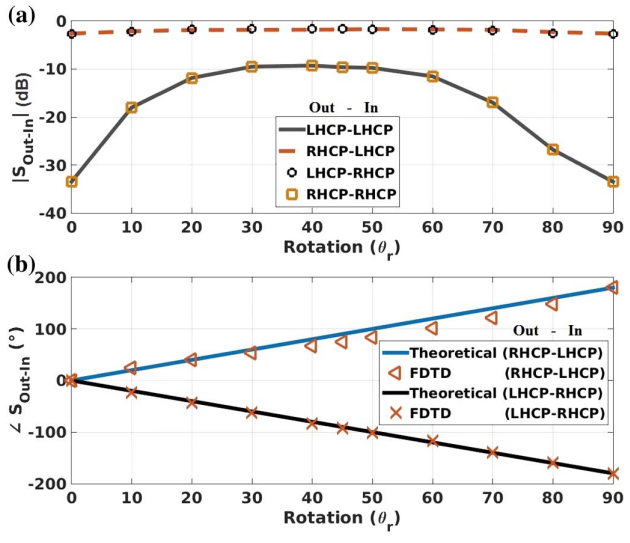

Fig. 4. FDTD simulation results for the transmission (a) amplitude and (b) phase variation with respect to the rotation angle θ for the normal incident CP waves. "Out" and "In" denote the handedness of transmitted and incident waves, respectively. Two layers of DSRLs are rotated identically.

reveal that the amplitudes of the cross transmission coefficients for CP incidence (LHCP–RHCP and LHCP–RHCP) are almost independent from the orientation angle of the unit-cell, and the insertion loss varies slightly with rotation angle from 1.7 to 2.62 dB. We also observe that the extinction ratio is better than 7.5 dB for all rotation angles. Therefore, by arranging the unit-cells with different orientations, it is possible to adjust the local spatial phase variation in such a way that it can effectively manipulate the impinging field for the desired operation. Due to the fact that any desired phase modification in the range of 0 to 2π can be achieved without any limitations only by arbitrary rotation, this method provides full control over the wavefronts.

3. RESULTS AND DISCUSSION

A. Anomalous Wavefront Bending

Here, we propose a MTS with individual elements rotated in such a way that the aperture can feasibly bend an incident CP wave. The characteristics of the flat MTS for the beam bending can be designed with the refraction phase shift in the y–z plane as follows [13,63]:

$$\phi(y) = \frac{2\pi}{\lambda} y \sin \theta_{\text{bending}}. \tag{4}$$

In order to realize a refraction with the bending angle of $\theta_{\text{bending}} = 30°$, the required phase profile $\varphi(y)$ is plotted as a solid blue line in Fig. 5. The supercell along the y-axis includes eight elements with rotation angles between 0 and π, and the unit-cells along the z-direction have the same rotation angle. The red dashed line in Fig. 5 corresponds to the phase distribution obtained by the FDTD simulation at the distance of 600 nm ($\approx 0.4\lambda$) after the structure under the LHCP incident wave. In Figs. 6(a) and 6(b), we simulate the transmitted electric field distribution for normal RHCP and LHCP illuminations, respectively. It can be observed that the bending angle of the transmitted electric field is almost 30° for both cases,

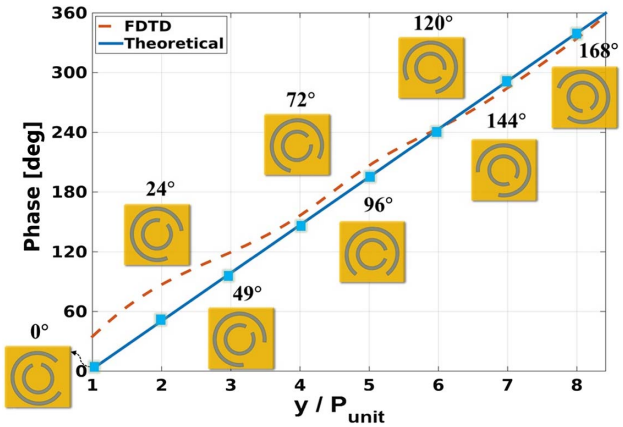

Fig. 5. Required phase discontinuity to bend the impinging LHCP plane wave with the refraction angle of 30° at the wavelength of 1550 nm. The solid blue line corresponds to the theoretical result which is obtained from Eq. (4), and the dashed red line is the numerical result at 600 nm after the structure under the LHCP incident wave. The square markers indicate the sampling of the phase profile using the eight elements with the step size of 415 nm along the y-axis.

which confirms the analytical approach. There is an important point which should be addressed regarding the bending difference in Figs. 6(a) and 6(b). For an incident RHCP (LHCP) beam, the major part of the light changes handedness to LHCP (RHCP) and experiences a phase pickup equal to -2θ (2θ) for clockwise rotation upon propagation through the structure. Therefore, it reveals the concept of anomalous refraction functionality for different hands of the circular polarization as shown in Figs. 6(a) and 6(b). Furthermore, this anomalous functionality can be observed if the rotating direction of the unit-cells is reversed when the lens is illuminated by a fixed incident polarization.

B. Bifunctional Wavefront Manipulation for Divergence and Convergence

In order to focus an incident CP plane wave, the MTS must actualize a spatially varying phase shift. The following expression, which can be derived by simple geometrical arguments, can describe the relationship between the required focusing behavior and the phase shift of each nanoantenna [13,63]:

$$\varphi(y) = \frac{2\pi}{\lambda}\left(\sqrt{f^2 + y^2} - f\right), \tag{5}$$

where f is the focal length. In our approach, the continuous phase function is approximated with discrete steps in the y-direction, and the unit-cells along the z-axis have the same rotation angle. The rotation of each quantized phase element is described by $\theta(y) = 0.5\varphi(y)$, where $\theta(y)$ is the rotation angle. Figure 7(a) illustrates the schematic of the designed 22-element focusing lens with clockwise rotation for the focal length of 2λ and the wavelength of 1550 nm. In Fig. 7(b), the required interfacial phase distribution is shown as a solid blue line, and the red dashed line indicates the full-wave FDTD simulation result for the realized phase distribution at a distance of 570 nm ($\approx 0.4\lambda$) after the aperture for the LHCP incident polarization. A great agreement is observed between FDTD and theoretical results.

The simulated field distribution at the operating frequency ($f = 193.5$ THz) reveals that the MTS lens can converge and diverge the cross polarization component. Figures 7(c) and 7(d) show the electric field distributions under the LHCP and RHCP incident waves, respectively. In Fig. 7(c), it can be

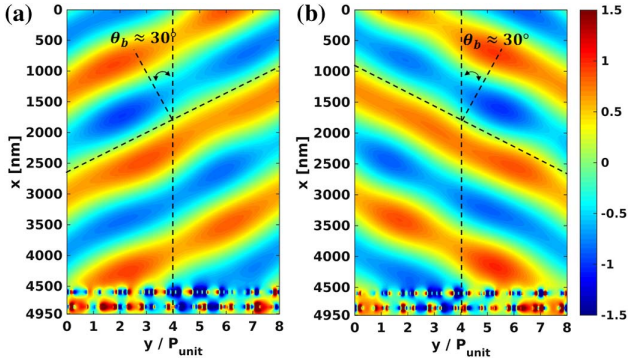

Fig. 6. FDTD simulated distributions of the real part of the cross polarized electric field for a metasurface composed of eight clockwise-rotated unit-cells with period of 415 nm under (a) RHCP and (b) LHCP incident waves.

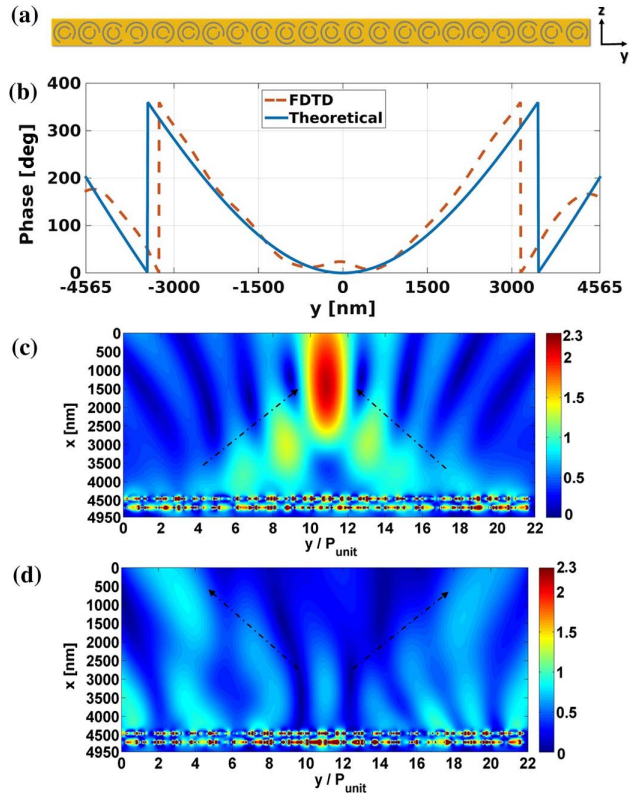

Fig. 7. (a) Schematic of the designed plasmonic MTS which contains 22 clockwise-rotated elements, (b) desired and realized phase discontinuities to carry out a focusing lens with the focal length of 2λ at the wavelength of 1550 nm under LHCP incident wave, and (c)–(d) distributions of the electric field amplitude for the LHCP and RHCP incident lights, respectively, which are obtained by full-wave FDTD simulation.

clearly seen that the MTS operates as a converging lens with focal length of $f = 2\lambda$ for the normal LHCP incident wave. Conversely, when the handedness of the CP incident wave is changed to RHCP, the proposed MTS behaves as a diverging lens as shown in Fig. 7(d). It is worth mentioning that if the DSRLs are rotated counterclockwise, the expected phase distribution, which is shown in Fig. 7(b), is changed from positive (convex shape) to negative (concave shape). Consequently, the lens causes the converging of the impinging RHCP wave and diverging of the LHCP light. To sum up, this single lens has the bifunctionality of convergence and divergence, which can be considered as a special privilege in comparison to the conventional lenses.

C. Flat-Top Beam

Here, we employ the theory of lossless beam shaping in order to investigate the possibility of mapping an initial irradiance distribution of a CP Gaussian beam at the plane $x = 0$ into a beam with uniform irradiance profile, which is called a flat-top beam, at the target plane $x = f_{\text{flat-top}}$. According to the geometrical optics (GO) theory, if we suppose the system does not absorb or block out the energy of the impinging beam (the energies of the incoming and outgoing waves are the same), it is possible to map a beam with arbitrary spatial distribution of $I(s)$ to a beam with desired irradiance profile of $Q(s)$. This analysis is carried out in three steps. The detailed discussions can be found in [64]. First, in order to satisfy the conservation of energy of the light beam, we define a normalization constant A which relates $I(s)$ to $Q(s)$, and it can be calculated as

$$A = \frac{\int_{-\infty}^{\infty} I(s)\mathrm{d}s}{\int_{-\infty}^{\infty} Q(s)\mathrm{d}s}. \tag{6}$$

Second, we determine the function of $\alpha(\zeta)$ which maps beams over the MTS to the beams at the target plane. This function can be obtained from [64]

$$\int_{-\infty}^{\zeta} I(s)\mathrm{d}s = A\int_{-\infty}^{\alpha(\zeta)} Q(s)\mathrm{d}s. \tag{7}$$

Equation (7) is another representation of the energy conservation, which means that the total energy of the rays with geometrical positions smaller than ζ must be equal to the energy of the rays at the target plane bounded by $\alpha(\zeta)$. In particular, Eq. (7) can be rewritten in a differential form as

$$Q(\alpha)\frac{d\alpha}{d\zeta} = \frac{1}{A}I(\zeta). \tag{8}$$

Finally, we determine the function $\varphi(\xi)$ that provides the phase shift introduced by beam shaping elements. By employing Fermat's principle and assuming that the total travelling time of a ray which comes from a distance of $x = -\infty$, passes through the lens, and ends up to a point at the focal plane should be stationary, the relation between $\varphi(\zeta)$ and $\alpha(\zeta)$ can be expressed as [64]

$$\frac{d\varphi}{d\zeta} = \alpha(\zeta). \tag{9}$$

The GO approximation is only valid for short wavelengths (high frequencies) where the diffraction effects are negligible. In order to examine the validity of the GO estimation, the dimensionless parameter of $\beta = (2\pi RD)/f\lambda$ is defined. R and D are the characteristic lengths of incoming and output beams, respectively. When β is large, the diffractive effect is negligible and the GO approximation is valid.

By enforcing Eqs. (6)–(9), the closed-form expression of the required phase distribution for converting a Gaussian beam to a flat-top beam can be achieved for the 1D case as [37–39,64]

$$\phi_y\left(\xi = \frac{\sqrt{2}y}{w_0}\right) = \beta_y\left(\frac{\sqrt{\pi}}{2}\xi\cdot\mathrm{erf}(\xi) + \frac{1}{2}\exp(-\xi^2) - \frac{1}{2}\right), \tag{10}$$

$$\beta_y = \frac{2\sqrt{2\pi}w_0 y_0}{f_{\text{flat-top}}\lambda}. \tag{11}$$

In Eq. (10), w_0 is the incident beam waist at $1/e$ peak intensity, y_0 is the half-width of the desired flat-top spot size, λ is the wavelength, $f_{\text{flat-top}}$ is the distance of the flat-top beam from the lens, and $\mathrm{erf}(\cdot)$ is the Gauss error function. The 2D problem can be easily separated to the product of two 1D cases in which the corresponding desired phase can be achieved by $\phi_{\text{tot}} = \phi_x(x) + \phi_y(y)$. The expected phase discontinuities for turning a Gaussian beam to a circular flat-top beam can be calculated with a similar approach as described in [64]:

$$\phi_{\text{tot}}\left(\xi=\frac{\sqrt{2}r}{w_0}\right)=\beta_r\left(\frac{\sqrt{\pi}}{2}\int_0^{\xi}\sqrt{1-\exp(-\rho^2)}\mathrm{d}\rho\right). \quad (12)$$

$$\beta_r=\frac{2\sqrt{2\pi}w_0r_0}{f_{\text{flat-top}}\lambda}, \quad (13)$$

where $r=\sqrt{x^2+y^2}$ is the radial distance from the optical axis and r_0 is the radius of the circular-shaped beam. In addition to this phase lens, Romero and Dickey demonstrate that a second focusing lens is necessary to perform the Fourier transform and create the desired flattened beam in the focal plane [37,64]. To achieve this functionality, we need to integrate the phase lens and the focusing lens in a single compact beam shaper metalens. The total phase function will then be [65,66]

$$\psi=\phi_{\text{tot}}-\frac{\pi r^2}{\lambda f_{\text{flat-top}}}. \quad (14)$$

In Eq. (14), the second term on the right-hand side comes from the focusing lens contribution. Consider the case in which a square spot is desired at the distance of $f_{\text{flat-top}}=10\lambda$ away from the optical system. The target spot dimension is $y_0=4\lambda$, and a laser is applied to produce a CP incident Gaussian beam with the waist of $w_0=3.87\lambda$. It is shown in Section 2 that the required phase profile, $\psi(y,z)$, can be generated by rotating the phase elements when the rotation angle is half of the required phase $[\theta(y,z)=0.5\psi(y,z)]$. A MTS including 81×81 array ($\approx22\lambda\times22\lambda$) is designed to realize a square-shaped flat-top beam with the aforementioned parameters.

Direct solution of the whole large array by a volume discretization technique, such as FDTD, is computationally expensive. As a result, we apply the field equivalence principle so from tangential fields on a surface in the vicinity of the array we can calculate the electromagnetic fields at any place in space [67]. Basically, we utilize FDTD with a local periodicity assumption to determine the field performance for each unit-cell and then collect the information for the field profile of the whole lens right after the MTS. The actual phase distribution of the array will be very similar to the theoretical prediction based on local periodicity as long as there is not a drastic phase change between the neighbor elements of the lens (which is usually the case); as such, the theoretical calculation can be used to determine the field profile of the whole array right after the MTS. Then, from this field profile it is possible to obtain the electric and magnetic fields at any point in space efficiently [14,68–70].

The required phase delay for the proposed design is plotted in Fig. 8(a). The amplitude of the electric field distribution for the LHCP incident Gaussian beam is sketched in Fig. 8(b). As expected, the handedness of the impinging beam is changed to RHCP and the flat-top beam is formed at $x=10\lambda$. The beam has relatively constant irradiance equal to 0.5 in a region with size of 6λ, and the shaped beam waist at $1/e$ peak intensity is 4.57λ. In Fig. 8(c), the electric field intensity is plotted in the y–z plane at the target plane, and it clearly shows the conversion of the CP Gaussian beam to the square-shaped flat-top beam in the presence of the lens. Figure 8(d) shows the intensity of a CP Gaussian beam in the y–z plane at $x=0$ with waist of $w_0=3.87\lambda$. The perfect flat-top beam can only be obtained

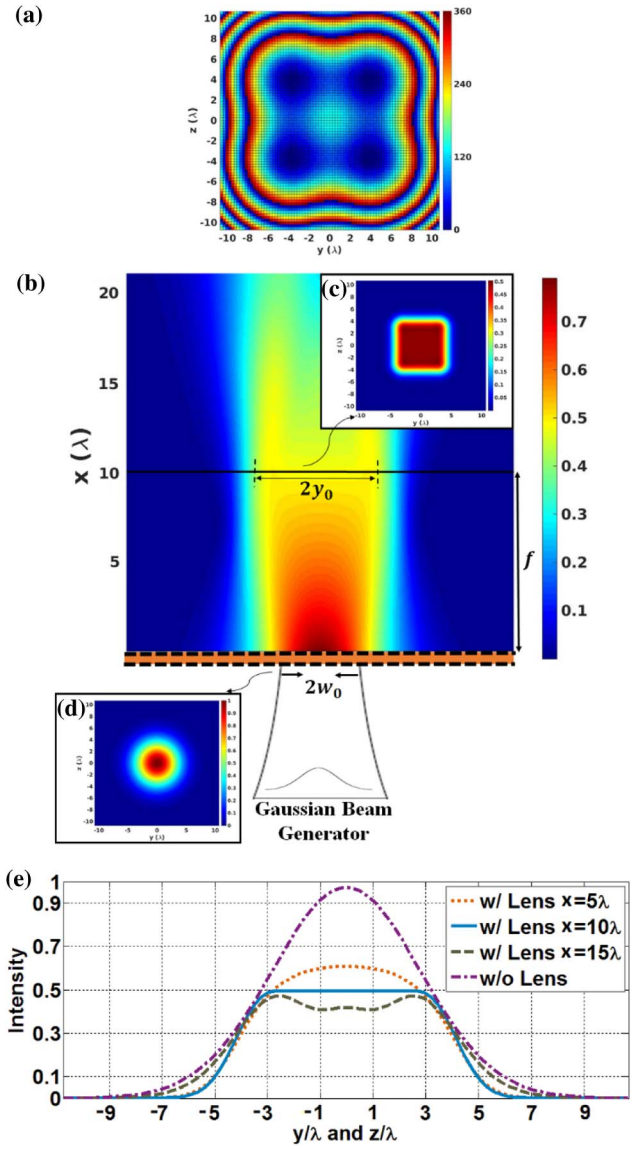

Fig. 8. (a) Required phase distribution for realizing a square shaped flat-top beam with 81×81 array of DSLRs with clockwise rotation. (b) Result for the propagation of the RHCP beam after the lens in the x–y plane. The flat top is found around 10λ as predicted by theory. 2D intensity patterns of (c) the square shaped flat-top beam and (d) the incident Gaussian beam. (e) The dashed–dotted line represents the field profile when the structure is absent. The dotted, solid, and dashed lines correspond to the intensity of RHCP electric field at different distances ($x=5\lambda$, 10λ, and 15λ) in the presence of the lens.

at the target plane, and the profile quickly deteriorates beyond it. In order to provide more clarification regarding this phenomenon, the transmitted cross polarized electric field intensity (RHCP) is plotted at different distances ($x=5\lambda$, 10λ, and 15λ) in the presence of the lens in Fig. 8(e). The dashed–dotted line corresponds to the intensity of the LHCP incident Gaussian beam in the absence of the structure at $x=10\lambda$. The flat-top beam quality can be controlled mainly by β. Low values of β cause the target spot to be more rounded with a wider skirt region. In contrast, the higher values of β lead

to an ideal uniform intensity profile with a narrow skirt and infinitely steep sides. It has been observed that the generation of an ideal flat-top beam is possible when $\beta > 4$. As is implied by Eq. (11), β can be increased by enlarging the target spot, reducing the wavelength, increasing the waist of the Gaussian beam, and shortening the focal length. On the other hand, by increasing β the phase profile varies more rapidly and the realization of the quantized domain becomes more challenging. Therefore, the quality of the target spot can be selected to be in line with the application [64]. Here, β is chosen to be equal to 7.76, which leads to a promising agreement between the designed and the realized parameters such as flat-top spot size and the position of the flattened beam.

Next, we investigate a structure with the same structural parameters as in the previous example except the required phase distribution on the lens is modified in such a way that a round-shaped flat-top beam can be formed at the target plane. The required phase pattern is obtained from Eqs. (12) to (14) and is plotted in Fig. 9(a). Figure 9(b) shows the intensity of the electric field distribution for a LHCP incident Gaussian beam in x–y plane. The position of the optimal flat-top beam is at $x = 10\lambda$ with the shaped beam radius of 3.21λ and the waist of 4.51λ, which is in good agreement with the predicted parameters by theory. Figure 9(c) is the 3D intensity display of the shaped beam in the focal plane of the lens. For comparison, Fig. 9(d) represents the intensity distribution of the incident Gaussian beam in the absence of the structure at the target plane. The shaped beam is observed to have a narrower skirt and an almost flat intensity distribution (≈0.56) at the top of the beam with small intensity variations.

The optical configuration which is presented cannot simultaneously provide both uniform amplitude and phase at the target plane. Therefore, the desired beam profile will be devastated after the target plane. The generation of a uniform

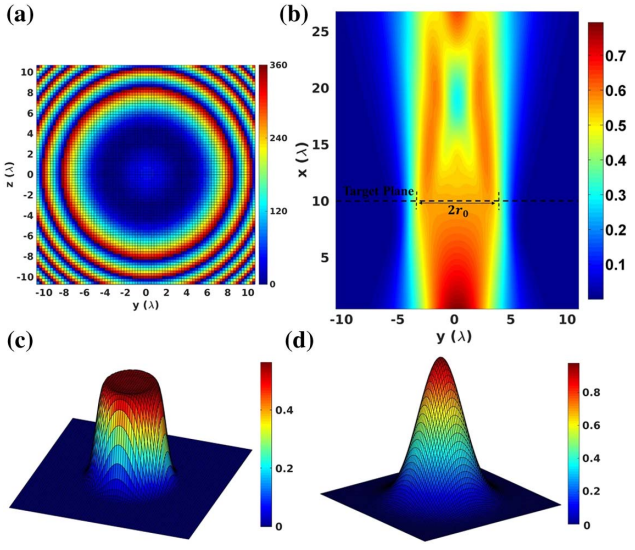

Fig. 9. (a) Required phase pattern to achieve a round-shaped flat-top beam with 81 × 81 array of DSLRs with clockwise rotation. (b) Distribution of the electric field amplitude for RHCP transmitted beam in the x–y plane. 3D intensity display of (c) the round-shaped flat-top beam and (d) the incident Gaussian beam at $x = 10\lambda$.

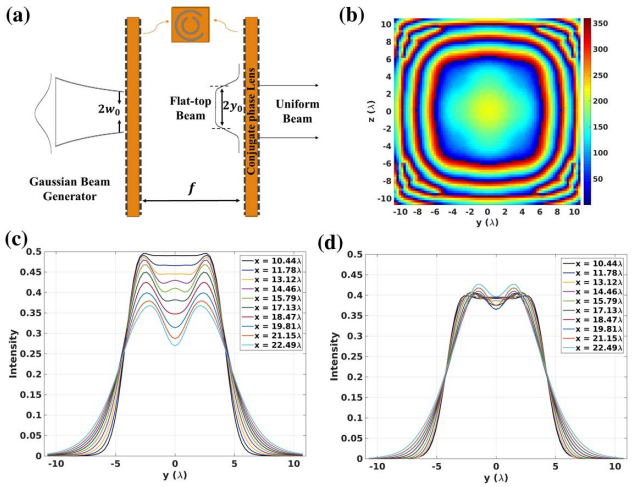

Fig. 10. (a) Optical system for creating a collimated uniform irradiance beam. (b) Phase distribution at the target plane of a square-shaped flat-top beam with $f = 10\lambda$, $y_0 = 4\lambda$, and $w_0 = 3.87\lambda$. Intensity of the generated flat-top beam at different distances after the target plane (c) without and (d) with the phase conjugate lens. One can see the performance becomes more collimated as the wave propagates.

phase and amplitude beam with the same handedness of the CP incident Gaussian beam is of particular interest. In this regard, it is possible to utilize a conjugate phase metalens which consists of DSLRs as building blocks at the target plane in order to modify the phase distribution in such a way that a uniform phase front can be obtained as well as a uniform amplitude profile. Thus, the uniform profile can propagate for considerable distances [64]. The optical system for generation of a collimated uniform irradiance beam is sketched in Fig. 10(a). As an example, the phase distribution of the beam at the target plane of Fig. 8 is obtained and plotted in Fig. 10(b). The phase of the conjugate phase lens is designed to cancel the phase of the uniform irradiance at the target plane of the beam shaping lens. Figures 10(c) and 10(d) represent the intensity of the flat-top beam at different distances after the target plane in the absence and presence of the conjugate phase lens, respectively. The influence of propagation on the change of the flat-top beam profile is more significant for the noncollimated beam [Fig. 10(c)]. For the collimated beam [Fig. 10(d)], the flat-top beam profile remains relatively unchanged for nearly 5λ beyond the target plane. In addition, the intensity of the collimated beam decays more smoothly than the noncollimated beam; thus it can propagate for more considerable distances. The only reason for deterioration of the collimated beam is the diffraction effects due to its finite size. In other words, the efficiency of collimating increases with the increment of flat-top spot size. It is worth noting that the collimated beam as an output of the designed optical system has the same handedness as the incident CP Gaussian beam.

4. CONCLUSION

In summary, the possibility of manipulating a CP beam by bilayer DSLRs at NIR wavelengths 1.55 μm is investigated.

It is shown that the array of DSLRs provides significant flexibility in designing various kinds of lenses with helicity dependency and space-variant phase shift. The physical mechanism behind the lens is based on the phase discontinuities that occur when an impinging CP incident beam is converted into the opposite handedness of circular polarization and experiences a geometrical phase pickup equal to twice the rotating angle of DSLRs. By controlling the handedness of the CP incident light and the rotation direction of the DSLRs, anomalous bending and bifunctional (convergence/divergence) MTSs are designed. The characteristics of the presented designs are validated with the full-wave simulation results obtained with the FDTD solver. In addition, we exploited the corresponding structure to convert a CP Gaussian beam into a uniform irradiance beam (flat-top beam). A compact flat-top beam shaper is proposed which combines the typical phase and focusing elements into a single optical metalens. In addition, a collimated uniform irradiance beam is realized by utilizing a conjugate phase lens at the target plane of the optical system. Thus, the uniform beam can propagate for longer distances beyond the target plane.

Funding. Air Force Office of Scientific Research (AFOSR) (FA9550-14-1-0349); Office of Naval Research (ONR) (N00014-10-1-0942.).

Acknowledgment. The authors would like to acknowledge Zhongliang Chen at Northeastern University Computer Architecture Research Group (NUCAR) for his help in data-parallelism and GPU architecting in order to facilitate the FDTD simulations. The authors are also grateful to the reviewers for their valuable comments. We appreciate the generous computing resources provided by the Northeastern University Discovery Cluster.

REFERENCES

1. V. G. Veselago, "The electrodynamics of substances with simultaneously negative values of ϵ and μ," Sov. Phys. Usp. **10**, 509–514 (1968).
2. J. Valentine, S. Zhang, T. Zentgraf, E. Ulin-Avila, D. A. Genov, G. Bartal, and X. Zhang, "Three-dimensional optical metamaterial with a negative refractive index," Nature **455**, 376–379 (2008).
3. V. M. Shalaev, "Optical negative-index metamaterials," Nat. Photonics **1**, 41–48 (2007).
4. J. B. Pendry, "Negative refraction makes a perfect lens," Phys. Rev. Lett. **85**, 3966–3969 (2000).
5. N. Fang, H. Lee, C. Sun, and X. Zhang, "Sub-diffraction-limited optical imaging with a silver superlens," Science **308**, 534–537 (2005).
6. S. Inampudi and V. A. Podolskiy, "Diffractive imaging route to sub-wavelength pixels," Appl. Phys. Lett. **102**, 241115 (2013).
7. A. Forouzmand, H. M. Bernety, and A. B. Yakovlev, "Graphene-loaded wire medium for tunable broadband subwavelength imaging," Phys. Rev. B **92**, 085402 (2015).
8. X. Zhang and Z. Liu, "Superlenses to overcome the diffraction limit," Nat. Mat. **7**, 435–441 (2008).
9. B. Edwards, A. Alù, M. G. Silveirinha, and N. R. Engheta, "Experimental verification of plasmonic cloaking at microwave frequencies with metamaterials," Phys. Rev. Lett. **103**, 153901 (2009).
10. J. B. Pendry, D. Schurig, and D. R. Smith, "Controlling electromagnetic fields," Science **312**, 1780–1782 (2006).
11. U. Leonhardt, "Optical conformal mapping," Science **312**, 1777–1780 (2006).
12. D. Schurig, J. J. Mock, B. J. Justice, S. A. Cummer, J. B. Pendry, A. F. Starr, and D. R. Smith, "Metamaterial electromagnetic cloak at microwave frequencies," Science **314**, 977–980 (2006).
13. J. Cheng, D. Ansari, and H. Mosallaei, "Wave manipulation with designer dielectric metasurfaces," Opt. Lett. **39**, 6285–6288 (2014).
14. B. Memarzadeh and H. Mosallaei, "Array of planar plasmonic scatterers functioning as light concentrator," Opt. Lett. **36**, 2569–2571 (2011).
15. M. Veysi, C. Guclu, O. Boyraz, and F. Capolino, "Thin anistropic metasurfaces for simultaneous light focusing and polarization manipulation," J. Opt. Soc. Am. B **32**, 318–323 (2015).
16. A. Silva, F. Monticone, G. Castaldi, V. Galdi, A. Alù, and N. Engheta, "Performing mathematical operations with metamaterials," Science **343**, 160–163 (2014).
17. M. Farmahini-Farahani, J. Cheng, and H. Mosallaei, "Metasurfaces nanoantennas for light processing," J. Opt. Soc. Am. B **30**, 2365–2370 (2013).
18. Y. Yang, W. Wang, P. Moitra, I. I. Kravchenko, D. P. Briggs, and J. Valentine, "Dielectric meta-reflectarray for broadband linear polarization conversion and optical vortex generation," Nano Lett. **14**, 1394–1399 (2014).
19. Y. Zhao and A. Alu, "Tailoring the dispersion of plasmonic nanorods to realize broadband optical meta-waveplate," Nano Lett. **13**, 1086–1091 (2013).
20. N. Yu, P. Genevet, M. A. Kats, F. Aieta, J.-P. Tetienne, F. Capasso, and Z. Gaburro, "Light propagation with phase discontinuities: generalized laws of reflection and refraction," Science **334**, 333–337 (2011).
21. X. J. Ni, N. K. Emani, A. V. Kildishev, A. Boltasseva, and V. M. Shalaev, "Broadband light bending with plasmonic nanoantennas," Science **335**, 427 (2012).
22. X. Ni, S. Ishii, A. V. Kildishev, and V. M. Shalaev, "Ultra-thin, planar, Babinet-inverted plasmonic metalenses," Light: Sci. Appl. **2**, e72 (2013).
23. A. Pors, M. G. Nielsen, R. L. Eriksen, and S. I. Bozhevolnyi, "Broadband focusing flat mirrors based on plasmonic gradient metasurfaces," Nano Lett. **13**, 829–834 (2013).
24. S. Sun, Q. He, S. Xiao, Q. Xu, X. Li, and L. Zhou, "Gradient-index meta-surfaces as a bridge linking propagating waves and surface waves," Nat. Mater. **11**, 426–431 (2012).
25. G. Li, M. Kang, S. Chen, S. Zhang, E. Y. B. Pun, K. W. Cheah, and J. Li, "Spin-enabled plasmonic metasurfaces for manipulating orbital angular momentum of light," Nano Lett. **13**, 4148–4151 (2013).
26. J. Lin, P. Genevet, M. A. Kats, N. Antoniou, and F. Capasso, "Nanostructured holograms for broadband manipulation of vector beams," Nano Lett. **13**, 4269–4274 (2013).
27. L. Huang, X. Chen, H. Mühlenbernd, H. Zhang, S. Chen, B. Bai, Q. Tan, G. Jin, K.-W. Cheah, C.-W. Qiu, J. Li, T. Zentgraf, and S. Zhang, "Three-dimensional optical holography using a plasmonic metasurface," Nat. Commun. **4**, 2808 (2013).
28. M. Farmahini Farahani and H. Mosallaei, "Functional graded-index metasurfaces for IR radiation and guiding," IEEE Trans. Nanotechnol. **14**, 75–81 (2015).
29. J. Cheng and H. Mosallaei, "Optical metasurfaces for beam scanning in space," Opt. Lett. **39**, 2719–2722 (2014).
30. M. Farmahini Farahani and H. Mosallaei, "A birefringent reflectarray metasurface for beam engineering in infrared," Opt. Lett. **38**, 462–464 (2013).
31. X. Li, S. Xiao, B. Cai, Q. He, T. J. Cui, and L. Zhou, "Flat metasurfaces to focus electromagnetic waves in reflection geometry," Opt. Lett. **37**, 4940–4942 (2012).
32. F. Monticone, N. M. Estakhri, and A. Alu, "Full control of nanoscale optical transmission with a composite metascreen," Phys. Rev. Lett. **110**, 203903 (2013).
33. X. Ding, F. Monticone, K. Zhang, L. Zhang, D. Gao, S. N. Burokur, A. d. Lustrac, Q. Wu, C.-W. Qiu, and A. Alu, "Ultrathin Panacharatnam–Berry metasurface with maximal cross-polarization efficiency," Adv. Mater. **27**, 1195–1200 (2015).
34. X. Chen, L. Huang, H. Mühlenbernd, G. Li, B. Bai, Q. Tan, G. Jin, C.-W. Qiu, S. Zhang, and T. Zentgraf, "Dual-polarity plasmonic metalens for visible light," Nat. Commun. **3**, 1198 (2012).

35. Z. Bomzon, G. Biener, V. Kleiner, and E. Hasman, "Space-variant Pancharatnam–Berry phase optical elements with computer-generated subwavelength gratings," Opt. Lett. **13**, 1141–1143 (2002).
36. E. Hasman, V. Kleiner, G. Biener, and A. Niv, "Polarization dependent focusing lens by use of quantized Pancharatnam–Berry phase diffractive optics," Appl. Phys. Lett. **82**, 328–330 (2003).
37. L. A. Romero and F. M. Dickey, "Lossless laser beam shaping," J. Opt. Soc. Am. A **13**, 751–760 (1996).
38. F. M. Dickey and S. C. Holswade, "Gaussian laser beam profile shaping," Opt. Eng. **35**, 3285–3295 (1996).
39. S. C. Holswade and F. M. Dickey, "Gaussian laser beam shaping: test and evaluation," Proc. SPIE **2863**, 237–245 (1996).
40. B. Memarzadeh and H. Mosallaei, "Engineering optical bistability in a multimaterial loop metasurface," J. Opt. Soc. Am. B **31**, 1539–1543 (2014).
41. B. Memarzadeh and H. Mosallaei, "Multimaterial loops as the building block for a functional metasurface," J. Opt. Soc. Am. B **30**, 1827–1834 (2013).
42. P. B. Johnson and R. W. Christy, "Optical constants of the noble metals," Phys. Rev. B **6**, 4370–4379 (1972).
43. M. Silveirinha, A. Alu, and N. Engheta, "Parallel-plate metamaterials for cloaking structures," Phys. Rev. B **78**, 075107 (2008).
44. H.-K. Yuan, U. K. Chettiar, W. Cai, A. V. Kildishev, A. Boltasseva, V. P. Drachev, and V. M. Shalaev, "A negative permeability material at red light," Opt. Express **15**, 1076–1083 (2007).
45. V. M. Shalaev, W. Cai, U. K. Chettiar, H.-K. Yuan, A. K. Sarychev, V. P. Drachev, and A. V. Kildishev, "Negative index of refraction in optical metamaterials," Opt. Lett. **30**, 3356–3358 (2005).
46. A. Boltasseva and V. M. Shalaev, "Fabrication of optical negative-index metamaterials: recent advances and outlook," Metamaterials **2**, 1–17 (2008).
47. J. Cho, M. Keung, N. Verellen, L. Lagae, V. Moshchalkov, P. Van Dorpe, and D. Gracias, "Nanoscale origami for 3D optics," Small **7**, 1943–1948 (2011).
48. B. Casse, H. Moser, J. Lee, M. Bahou, S. Inglis, and L. Jian, "Towards three-dimensional and multilayer rod-split-ring metamaterial structures by means of deep x-ray lithography," Appl. Phys. Lett. **90**, 254106 (2007).
49. B. Lahiri, A. Khokhar, R. De La Rue, S. McMeekin, and N. Johnson, "Asymmetric split ring resonators for optical sensing of organic materials," Opt. Express **17**, 1107–1115 (2009).
50. D. Lin, P. Fan, E. Hasman, and M. K. Brongersma, "Dielectric gradient metasurface optical elements," Science **345**, 298–302 (2014).
51. R. Phillion and M. Okoniewski, "Lenses for circular polarization using planar arrays of rotated passive elements," IEEE Trans. Antennas Propag. **59**, 1217–1227 (2011).
52. M. Veysi, C. Guclu, and F. Capolino, "Vortex beams with strong longitudinally polarized magnetic field and their generation by using metasurfaces," J. Opt. Soc. Am. B **32**, 345–354 (2015).
53. M. Euler, V. Fusco, R. Cahill, and R. Dickie, "Comparison of frequency-selective screen-based linear to circular split-ring polarisation convertors," IET Microw. Antennas Propagat. **4**, 1764–1772 (2010).
54. S. Yan and G. A. E. Vandenbosch, "Compact circular polarizer based on chiral twisted double split-ring resonator," Appl. Phys. Lett. **102**, 103503 (2013).
55. N. Katsarakis, T. Koschny, M. Kafesaki, E. Economou, and C. Soukoulis, "Electric coupling to the magnetic resonance of split ring resonators," Appl. Phys. Lett. **84**, 2943–2945 (2004).
56. P. Gay-Balmaz and O. Martin, "Electromagnetic resonances in individual and coupled split-ring resonators," J. Appl. Phys. **92**, 2929–2936 (2002).
57. M. Alizadeh and B. Reinhard, "plasmonically enhanced chiral optical fields and forces in achiral split ring resonators," ACS Photon. **2**, 361–368 (2015).
58. L. Wu, Z. Yang, Y. Cheng, M. Zhao, R. Gong, Y. Zheng, J. Duan, and X. Yuan, "Giant asymmetric transmission of circular polarization in layer-by-layer chiral metamaterials," Appl. Phys. Lett. **103**, 021903 (2013).
59. Y. Ye, X. Li, F. Zhuang, and S. Chang, "Homogeneous circular polarizers using a bilayered chiral metamaterial," Appl. Phys. Lett. **99**, 031111 (2011).
60. C. Huang, Y. Feng, J. Zhao, Z. Wang, and T. Jiang, "Asymmetric electromagnetic wave transmission of linear polarization via polarization conversion through chiral metamaterial structures," Phys. Rev. B **85**, 195131 (2012).
61. Y. Zhao and A. Alu, "Manipulating light polarization with ultrathin plasmonic metasurfaces," Phys. Rev. B. **84**, 205428 (2011).
62. D. Zelenchuk and V. Fusco, "Split-ring FSS spiral phase plate," IEEE Antennas Wireless Propag. Lett. **12**, 284–287 (2013).
63. M. M. Salary, M. Nazari, and H. Mosallaei, "Robust technique for computation of scattering and absorption of light by array of nanowires on layered substrate," J. Opt. Soc. Am. B **32**, 2448–2461 (2015).
64. F. Dickey and S. Holswade, *Laser Beam Shaping* (Marcel Dekker, 2000).
65. X. G. Huang, M. R. Wang, and C. Yu, "High-efficiency flat-top beam shaper fabricated by a nonlithographic technique," Opt. Eng. **38**, 208–213 (1999).
66. J. A. Hoffnagle, "A new derivation of the Dickey–Romero–Holswade phase function," Proc. SPIE **5876**, 587606 (2005).
67. R. F. Harrington, *Time-Harmonic Electromganetic Fields* (Wiley, 2001).
68. L. Verslegers, P. B. Catrysse, Z. Yu, W. Shin, Z. Ruan, and S. Fan, "Phase front design with metallic pillar arrays," Opt. Lett. **35**, 844 (2010).
69. A. Ahmadi, S. D. Ghadarghadr, and H. Mosallaei, "An optical reflectarray nanoantenna: the concept and design," Opt. Express **18**, 123–133 (2009).
70. C. G. M. Ryan, M. R. Chaharmir, J. Shaker, J. R. Bray, Y. M. M. Antar, and A. Ittipiboon, "A wideband transmitarray using dual-resonant double square rings," IEEE Trans. Antennas Propag. **58**, 1486–1493 (2010).